

DYNAMIC FINITE ELEMENT SIMULATION OF WHEEL–RAIL CONTACT RESPONSE FOR THE CURVED TRACK CASE

Xiongfei ZHOU, Lin JING*, Xiaoqi MA

State Key Laboratory of Traction Power, Southwest Jiaotong University, Chengdu, China

Submitted 14 April 2020; resubmitted 24 June 2020; accepted 9 August 2020

Abstract. The wheel–rail interaction will be intensified on account of the complexity of the wheel–rail contact geometry on a curved track. It also may become more complicated and/or have significant difference as the train speed increases, since the dynamic effects cannot be ignored then. In this study, based on explicit Finite Element (FE) software LS-DYNA 971, a Three-Dimensional (3D) elastic-plastic FE model was built to simulate the dynamic wheel–rail contact behaviour of curve negotiating, where the superelevation and roll angle as well as the strain rate effect were considered. The evolution of contact patch and pressure, wheel–rail contact force, the stress/strain state and the acceleration of the axle were employed to examine the wheel–rail transient dynamic response. Furthermore, the influences of axle load, curve radius and strain rate effect were also discussed. It is found that the maximum vertical contact force, contact pressure, stress and strain on the curved track increase with the decreasing curve radius, and they increase with the increasing axle load except for lateral contact force. The wheel–rail dynamic responses on the curved track are significantly enhanced compared to the straight track. Moreover, the strain rate effect can enhance von-Mises stress and contact pressure, suppress the plastic deformation of the rail and wheel, but it has little effect on the vertical and lateral contact forces and stable acceleration of axle. The Rate-Sensitive Factors (RSF) of the wheel and rail on the curved track are weaker than those on the straight track. These findings will be very helpful to study the competitive relationship between the rolling contact fatigue and wear, as well as the crack initiation and propagation problem.

Keywords: wheel–rail interaction, curved track, dynamic response, strain-rate effect, finite element analysis.

Notations

3D – three-dimensional;
AOA – attack of angle;
FE – finite element;
RSF – rate-sensitive factors;
SRC – strain rate parameter C ;
SRP – strain rate parameter P .

Introduction

As an economic, safe and environmentally friendly means of transportation, high-speed railway transportation is increasingly favoured by people. But with the continuous increase of urban rail transit lines with small radius curves and the coupling of high speed and large axle load, the problems caused by the train passing through the curved track are increasingly prominent, such as wear, fatigue and fracture (Wang *et al.* 2009), which seriously affects the service life of the wheel and rail and greatly increases

the economic costs. At the same time, the wheel–rail system as a core of the vehicle/track coupling system, will directly influence the safety, stability and ride comfort of the train (Zhai *et al.* 2009). When the train negotiates a curved track, the centerline of wheelset will deviate significantly from the centerline of track, due to its self-steering ability, making the wheel–rail contact geometry more complicated than that on a straight track. Otherwise, the superelevation should be applied on the outer rail to neutralize centrifugal force of vehicle curve negotiation, which is confirmed by the vehicle speed and the radius of curvature. The poor performance of curve negotiation will aggravate the wheel–rail interaction, resulting in a series of problems such as gauge widening and rail over, which greatly increases the maintenance workload of the track and even endangers the safety of operation (Wang *et al.* 2014). Therefore, it is quite essential to understand well the dynamic wheel–rail responses of curve negotiation.

*Corresponding author. E-mail: jinglin@swjtu.edu.cn

The wheel–rail dynamic behaviour curved track has been widely investigated experimentally, numerically, and theoretically in the past few decades. Matsumoto *et al.* (1996, 2006) developed a full-scale bogie test rig that simulates curve conditions and subsequently improved it. The results of experiments agreed well with the Kalker's linear theory (Kalker 1967, 1973), and it revealed that a small change in the lateral displacement of wheelset may lead to a great change in creep characteristics of wheel–rail system. Recently, Liu *et al.* (2018a) conducted the field experiment of heavy-haul locomotive on a curved track to investigate the vertical dynamic loads, verifying the validation of the proposed theoretical model. As for theoretical analyses, based on the linear creep theory (Kalker 1967), Newland (1968) and Boocock (1969) put forward the mechanism of creeping force guidance, and a quasi-static method was employed to examine curve negotiation mechanism. Elkins and Gostling (1977) studied the steady-state curving performance of the vehicle based on the Kalker's simplified nonlinear creep theory (Kalker 1973). For the non-conformal contact of the wheel–rail, some classic theories, such as Hertzian theory (Hertz 1882) and Kalker's theory (Kalker 1973) are introduced to analyse the wheel–rail contact problem. Nevertheless, the wheel/rail is more prone to conformal contact on curve negotiation, such as the wheel flange in contact with rail gauge. The above theory will be not accurate on a curved track due to the assumption of linear elastic half-space.

With the development of computer technology, lots of studies on the vehicle /track dynamic response were performed based on the multi-body dynamic model and FE simulation. The multi-body dynamics means and numerical integration methods are widely adopted in dynamic wheel–rail interaction and performance matching of the straight or curved tracks (Zboiński 1998; Rezvani *et al.* 2009; Dailydka *et al.* 2008; Ma *et al.* 2015; Mosayebi *et al.* 2016, 2017). Liu *et al.* (2018b) employed the periodic structure theory to investigate the dynamic response of the curved track under non-moving and moving harmonic load conditions and drew the conclusion that dynamic response of the track is greatly affected when the radius of curvature becomes small. However, the FE method has been verified to outperform the multi-body dynamic approach in studying the dynamic wheel–rail rolling contact behaviour due to the strong nonlinearities of the geometry, contact, and material. A great number of FE models have been adopted to study wheel–rail dynamic response including contact stress and contact force on straight track up to now (Jing, Han 2017; Han *et al.* 2018; Zhao, Li 2011; Vo *et al.* 2014; Zakeri, Tajalli 2018). The FE analysis of wheel–rail dynamic response for curved track case is scarce, but the research on 2-point and conformal contact is common. Sladkowski and Sitarz (2005) investigated the distributions of multi-point contact zones and stresses, including the wheel tread/rail head contact and flange/rail gauge contact. Telliskivi and Olofsson (2001) studied the flange/rail gauge contact stress by building the FE model. Kaewunruen *et al.* (2019) utilized a FE package STRAND7

(<https://www.strand7.com>) to create 3D curved track model and examined the dynamic response of the curved track by applying a moving load, but the wheel–rail contact behaviour was not considered. It is often necessary to establish a long enough track model to reflect the characteristics of the curve, which will greatly increase the number of mesh and extend the computation time, especially for large radius curved track. Therefore, a small section of track passed by the wheelset in a short period of time is approximately regarded as a straight track to improve the computational efficiency. On the basis of above principle, Vo *et al.* (2015) adopted the FE method considering the AOA and superelevation to analyse stress state and damage of the rail on the curved track, but not taking the roll angle into account. Yang *et al.* (2016) built a straight track and half-wheelset model, simulating the transition process of wheel rolling on the rail from single-point tread contact to 2-point tread-flange contact. From the above literature, it is reasonable to simulate the wheel–rail transient dynamic response of the vehicle passing through the curved track by means of a straight track model. However, the roll angle is rarely considered and the influence of strain rate effect of wheel/rail materials on the wheel–rail dynamic response for the curved track case have not been distinctly clarified up to now.

By accounting for more realistic contact condition, the FE method has been demonstrated to be effective and accurate for solving wheel–rail contact problem. As the train speed improves, the strain rate effect of materials cannot be ignored (Jing *et al.* 2017, 2022a, 2022b; Liu *et al.* 2018a, 2018b; Su *et al.* 2020; Zhou *et al.* 2022). Hence, in the present work, the wheel–rail dynamic interaction of curve negotiation was investigated by employing the FE model of a wheelset in contact with double rails, where the strain rate effect of wheel/rail materials, superelevation, the roll angle and initial lateral displacement were fully considered. The influences of the curve radius, axle loads and strain rate effect on the dynamic wheel–rail contact behaviour were investigated.

1. FE modelling

1.1. Model description

There are a series of components or systems work together on vehicle curve negotiation, such as primary suspension system, secondary suspension system, car body, bogie, etc. However, the performance of curve negotiation is always reflected on the wheel–rail contact behaviour. Meanwhile, wheel–rail rolling contact has asymmetry due to the contact geometry, transient contact location and contact load, especially for the curved track condition. Therefore, a 3D FE model of the wheelset was created to investigate the dynamic wheel–rail response of curve negotiating. In order to save calculation time and cost, we adopted a simplified method to approximate the small segment of the track through which the wheelset passes in a short period of time as a straight segment, as employed in research by

Vo *et al.* (2015). The FE model was developed with the straight track, but to truly reflect the dynamic wheel–rail contact relationship of curve negotiating, the superelevation, the rail cant, the initial lateral displacement of the wheelset and the roll angle were considered. The present simulation is a wheelset turning to right, as shown in Figure 1a. From the perspective of the train driver, the left side is defined as the higher rail (outer rail), and the right side is defined as the lower rail (inner rail). The geometric models of S1002CN tread and 60 kg/m rail were established by SOLIDWORKS software (<https://www.solidworks.com>), and then combined with commercial FE code HYPERMESH/LS-DYNA (<https://www.ansys.com/products/structures/ansys-ls-dyna>) for further study. And the rail cant was set to 1 in 40 according to realistic operation conditions in Chinese Railways, and the superelevation was considered, see Section 1.3. The schematic of the FE model of wheel–rail system is illustrated in Figure 1b.

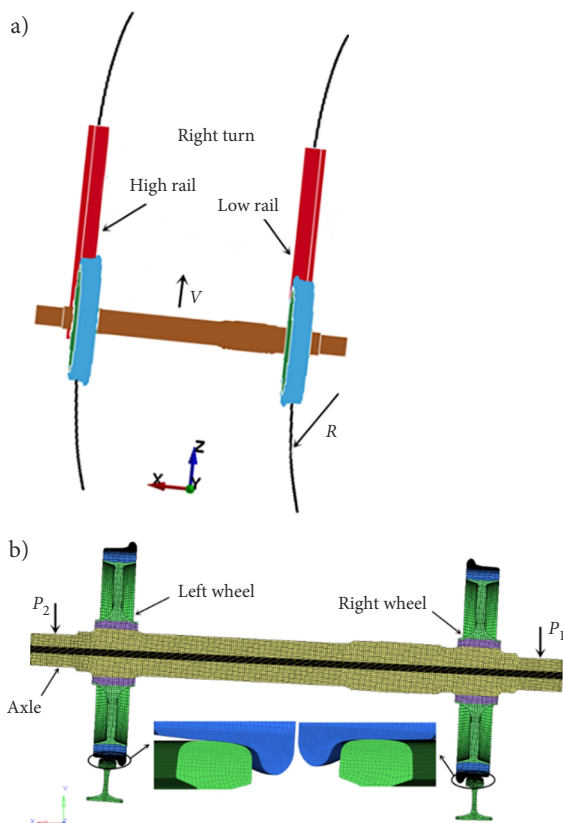


Figure 1. Geometrical modelling of the wheelset rolling on a curved track: a – diagram of right turn of the wheelset; b – sectional view of the FE model

The wheel radius is 430 mm and the length of track is 2 m, which are simulated with the 8-node solid elements. To achieve the balance of computational accuracy and efficiency, a non-uniformed mesh method was established, where the contact area of wheel–rail was fine meshed (1×1 mm) and the far-contact regions of wheel–rail was coarsely meshed (2×2 mm). The wheel–rail system includes a total of 6439961 nodes and 5956372 elements.

1.2. Boundary conditions and material properties

In the model, a 3D Cartesian coordinate was established with the axes of x , y , z , which represent lateral, vertical, and longitudinal directions, respectively. Degree-of-freedom of all nodes at the bottom of the rail were fully constrained to represent the clamped boundary conditions, both ends of the axle were not restricted to ensure the dynamic curve passing performance. The mechanical parameters of the wheel–rail components were presented in Table 1, the detail of which can be seen in researches by Jing *et al.* (2016, 2017); Ma *et al.* (2018), and the plastic kinematic hardening model in LS-DYNA 971 was used. The strain-rate effect of wheel/rail materials was taken into account by Cowper–Symonds model, given as:

$$\frac{\sigma_d}{\sigma_s} = 1 + \left(\frac{\dot{\epsilon}}{C} \right)^{\frac{1}{P}}, \quad (1)$$

where: $\dot{\epsilon}$ is the strain rate; σ_s , σ_d are the quasi-static and dynamic yield stresses, respectively; C , P are the rate-dependent factors, corresponding to the SRC and SRP options of the material properties in LS-DYNA 971, respectively.

In the present work, the rate-dependent parameters were set as: $C = 1.15 \cdot 10^8 \text{ s}^{-1}$ and $P = 6.617$ for the wheel rim and $C = 9.6117 \cdot 10^4 \text{ s}^{-1}$ and $P = 4.088$ for the rail steel, according to the corresponding dynamic experimental results (Su *et al.* 2020).

For sake of focusing on the dynamic response of wheel–rail contact, the elastic-plasticity of the axle is reasonably neglected. Instead, it was represented by the material model *MAT_RIGID. Actually, the vertical load applied to the both sides of wheelset should change with time due to the mutual vibration of the train and track (Vo *et al.* 2015). In the present work, we pay attention to the transient dynamic response of wheel–rail and the traveling time of the wheel is very short. Hence, the force P_1 and P_2 exerted on the right and left sides of a wheelset can be considered to be constant during a short time and can be

Table 1. The mechanical parameters of the wheel–rail components

Component	Elastic modulus [GPa]	Density [kg/m ³]	Poisson ratio	Yield stress [MPa]	Tangent modulus [GPa]
Rim	213	7800	0.3	561	21
Web	216	7800	0.3	395	21
Hub	213	7800	0.3	417	21
Axle	206	7575	0.3	560	20
Rail	193	7800	0.3	525	19

calculated according to the criteria of the standard BS EN 13104:2009+A1:2010. For example, under 17 t axle load, the larger force P_1 is equal to 110.41 kN and the smaller force P_2 is equal to 77.56 kN. In addition, the translational velocity v was applied to the wheel and axle, while the relevant rotational velocity ω was exerted on the wheel according to $v = \omega \cdot R$. An automatic surface-to-surface contact algorithm was adopted for the entire wheel-rail system.

1.3. Input of simulation parameters

The simulated axle loads are 16, 17 and 18 t, respectively. According to the design of high-speed railway in China (TB 10621-2014), the curve radius of 2800 and 4000 m are used as the minimum curve radius for high-speed trains to pass under design speeds, so $R = 2800$ m and $R = 4000$ m are selected and a straight track with an infinite radius of curvature was chosen for comparison. The simulated train speed was set to 130 km/h in the present work. While the train negotiating the curved track in steady state, the wheelset deviates from track centerline will make the rolling circle radius of the left and right wheels different, resulting in a certain amount of lateral displacement and roll angle of the wheelset. The following equations can be obtained by geometric methods (Boocock 1969):

$$\frac{R}{r_0} = \frac{R+b}{r_l}; \quad (2)$$

$$r_0 = \frac{r_l + r_r}{2}, \quad (3)$$

where: r_0 is radius of the nominal rolling circle; r_l , r_r are radius of rolling circle for the left and right wheel, respectively; R is the radius of curved track; b is half the distance between wheel rolling circles.

Combining Equation (3) with Equation (2), yields:

$$r_l - r_r = \frac{2 \cdot r_0 \cdot b}{R}. \quad (4)$$

Then, the equivalent conicity λ can be defined as (Boocock 1969):

$$\lambda = \frac{r_l - r_r}{y}, \quad (5)$$

where: y represents the lateral displacement of a wheelset.

From Equations (4) and (5), y can be written as:

$$y = \frac{r_0 \cdot b}{\lambda \cdot R}. \quad (6)$$

Otherwise, on condition that the wheel S1002CN is in rigid contact with the 60 kg/m rail, the relationships between the equivalent conicity λ and the lateral displacement of a wheelset y , and the roll angle ϕ versus y are depicted in Figure 2. Hence, combined with Equation (6), the FE simulation parameters of curve negotiation in the steady state can be obtained. Here, the lateral displacement of the wheelset to the right is negative and to the

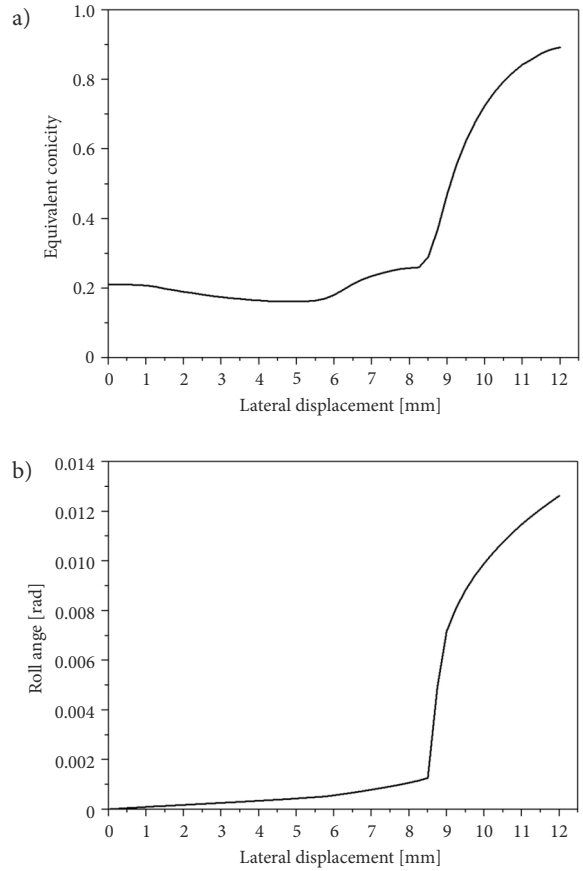


Figure 2. Geometric relation of the rigid wheel-rail contact of the wheelset: a – equivalent conicity versus lateral displacement; b – roll angle versus lateral displacement

Table 2. Inputting parameters in FE simulations of curve negotiation model

Radius of curved track [m]	Train speed [km/h]	Superelevation [mm]	Wheelset lateral displacement [mm]	Roll angle [rad]
2800	130	75	1.13	0.0041
4000	130	50	0.75	0.0061
∞	130	0	0	0

left is positive. In the model, the wheel turns right along the direction of travel. Therefore, the right side is the inner rail and the left side is the outer rail with superelevation. The input parameters of curved track model are presented in Table 2.

2. Results and discussion

In the section, the obtained simulated results with respect to contact patch, contact pressure, contact force, strain and stress, and acceleration response of the axle are discussed in detail. The influence of strain rate on rail and wheel is analysed emphatically on a curved track.

2.1. Contact patch and contact pressure

The contact area is determined by the distribution of nodal pressure on the rail, and the pressure amplitude in the contact zone should be greater than zero. The evolution of the dynamic rolling contact patch as the wheelset passed through the curved track under higher rail and lower rail is investigated (Figure 3). It is observed that the wheel and rail are always in contact for the straight track condition, but they will be temporarily out of contact on higher rail (left rail) for the curved track condition, which is exactly when the wheel–rail contact force of left side is almost zero in Figure 7a. Moreover, the left wheel and left rail will be in contact more earlier under the condition of a curvature radius of 4000 m than a curvature radius of 2000 m due to the different initial displacement and superelevation. It can be observed that the left wheel and rail will be out of contact again at about 7 ms. The wheel–rail contact is only temporarily lost, which does not necessarily lead to train derailment. As the derailment of the train is the result of the coupling of contact force and contact time under dynamic rolling contact. At the same moment, the larger contact pressure always occurs on the right rail under the straight case, and it will exhibit alternating changes on the left and right rails under curve negotiation. During the simulation time, the maximum contact pressure occurs at 7 ms or so under straight condition. However, in the case of curved track, the maximum contact pressure appears at approximately 2.5 ms. The typical non-Hertz contact patch occurs during rolling

of the wheel on the rail due to the non-constant contact surface curvatures.

To gain an insight into the effect of strain rate to contact pressure, the maximum contact patch and the 3D distribution of contact pressure with 2 material models under different conditions are illustrated in Figure 4 and Figure 5, respectively. By counting the number of element mesh, it can be reflected that the contact patch area under curved track conditions is significantly smaller than that under straight track conditions. However, there is no occurrence of 2 contact spots on the inner rail, which is different from the phenomenon in the research by Vo *et al.* (2015), due to the influence of attack angle. In addition, the contact patch area obtained by considering the strain rate model is significantly smaller than the model does not include the strain rate under the same working conditions. The strain rate effect can influence the plastic flow of the wheel–rail material, resulting in reducing the area of contact patch and increasing the contact interface pressure. Figure 6 systematically compares the maximum contact interface pressure under different operating conditions and material models. It can be perceived that as the radius of the curve decreases, the wheel–rail contact pressure will disproportionately increases sharply, causing a large increase in the wheel/rail wear. Otherwise, wheel flange/rail gauge contact is more likely to occur on the small curvature radius track, threatening the running safety performance of vehicles. The strain rate increases the maximum contact pressure from 19 to 25 MPa under the same conditions.

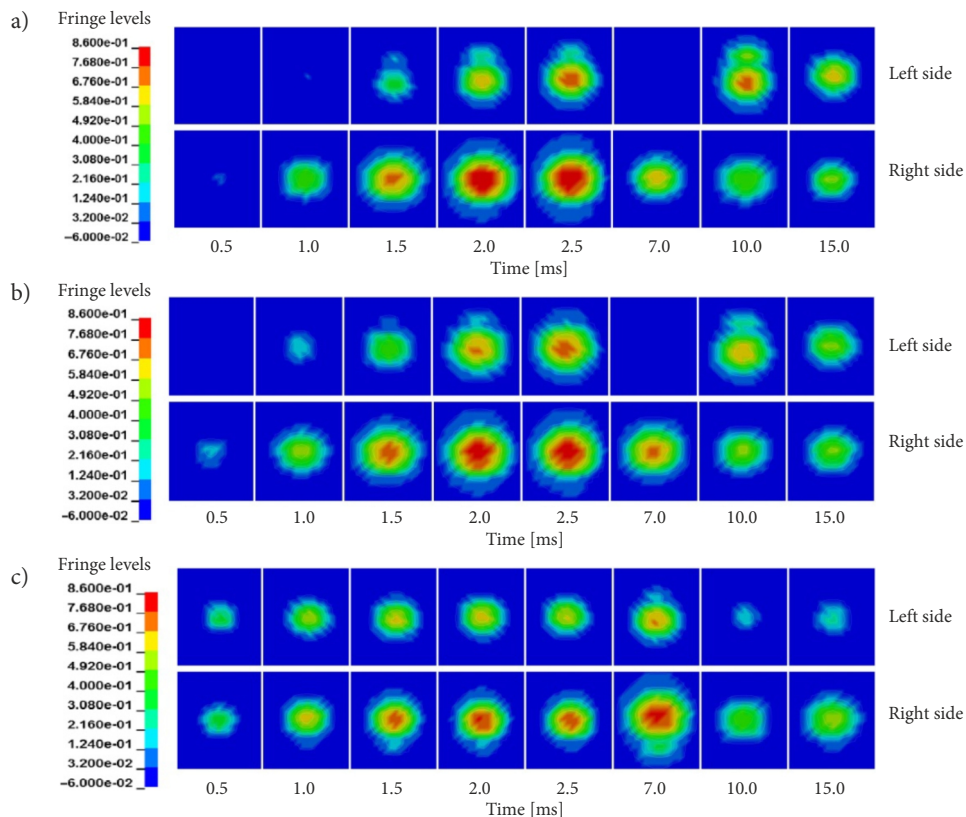


Figure 3. The evolution of the contact patch under the axle load of 17 t for the curved track cases with different radius of curvature: a – $R = 2800$ m; b – $R = 4000$ m; c – $R = \infty$

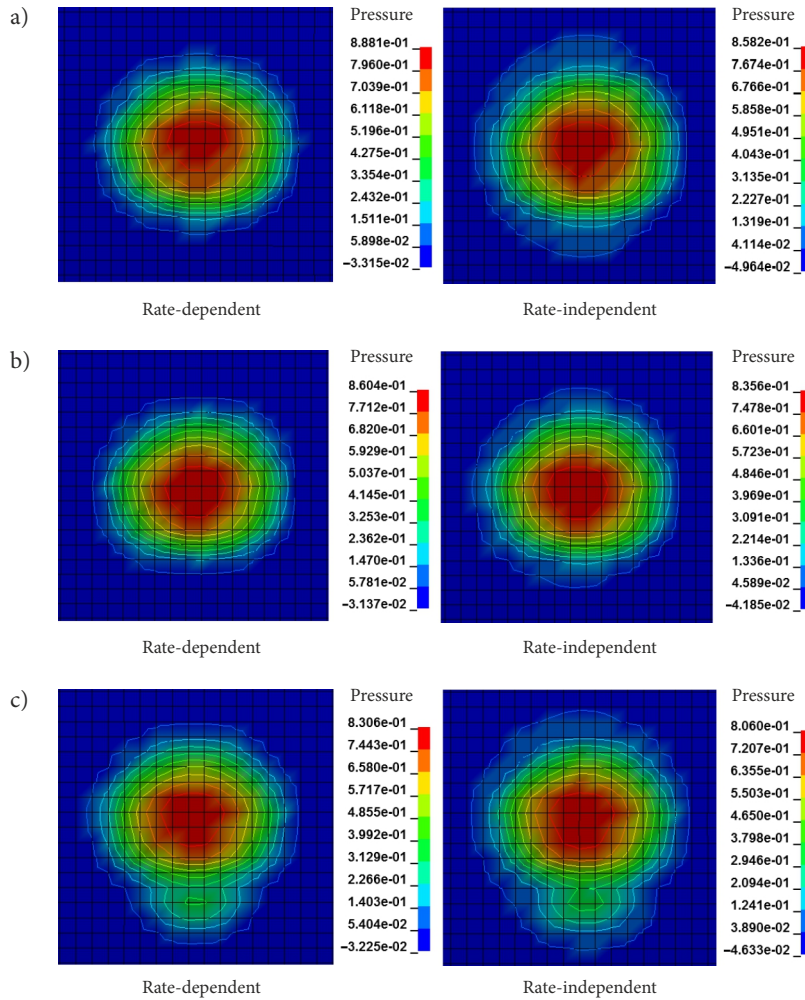


Figure 4. Contours of nodal pressure on the rail under axle load of 17 t for the different curvature radii: a – $R = 2800$ m; b – $R = 4000$ m; c – $R = \infty$

2.2. Wheel–rail contact force

For typical condition with the axle load of 17 t and the curvature radius of 2800 m, the wheel–rail contact force history curves are plotted in Figure 7. It can be seen that wheel–rail contact force does not obviously tend to stabilize over time, which is different from the straight case (Ma *et al.* 2018). There is a certain phase difference in contact force between left and right sides. In addition, the maximum vertical contact force appears on the first peak value, the maximum lateral and longitudinal contact force occur on the second peak value. Regardless of whether the strain rate of the material is considered, the vertical and lateral contact force history curves are consistent. The strain rate effect has an effect on the peak value of longitudinal contact force, but has no influence on the moment when the peak value of contact force occurs.

To further examine the effect of superelevation to the higher rail (left side) and lower rail (right side), Figure 8 shows the maximum wheel–rail contact force for both sides under different axle loads and curvature radius. It is seen that the wheel–rail contact force is largely enhanced under a curved track, besides the lateral contact force of left side. What is different from the straight condition,

the lateral wheel–rail contact force on both sides is in the same direction to provide a part of its centrifugal force when vehicle negotiating the curved track. The absolute values of maximum wheel–rail contact force solved by 2 material models are presented in Figure 9. The maximum vertical and longitudinal contact force increase monotonously with the axle load, the lateral contact force is less sensitive to the axle load. On the small curvature radius track, the maximum wheel–rail contact force in 3 directions increases significantly, which aggravates the wheel–rail interaction. Likewise, strain rate effect has no influence on the maximum vertical and lateral contact, the longitudinal contact force has certain sensitivity to the strain rate.

2.3. Wheel–rail rolling contact stress and strain states

In the frictionless contact surface, the dynamic response of wheel–rail of curve negotiation will be influence by the superelevation. Therefore, the stress and strain states of higher rail and lower rail are investigated in this section. Furthermore, the strain rate hardening effect of the wheel and rail is discussed in detail.

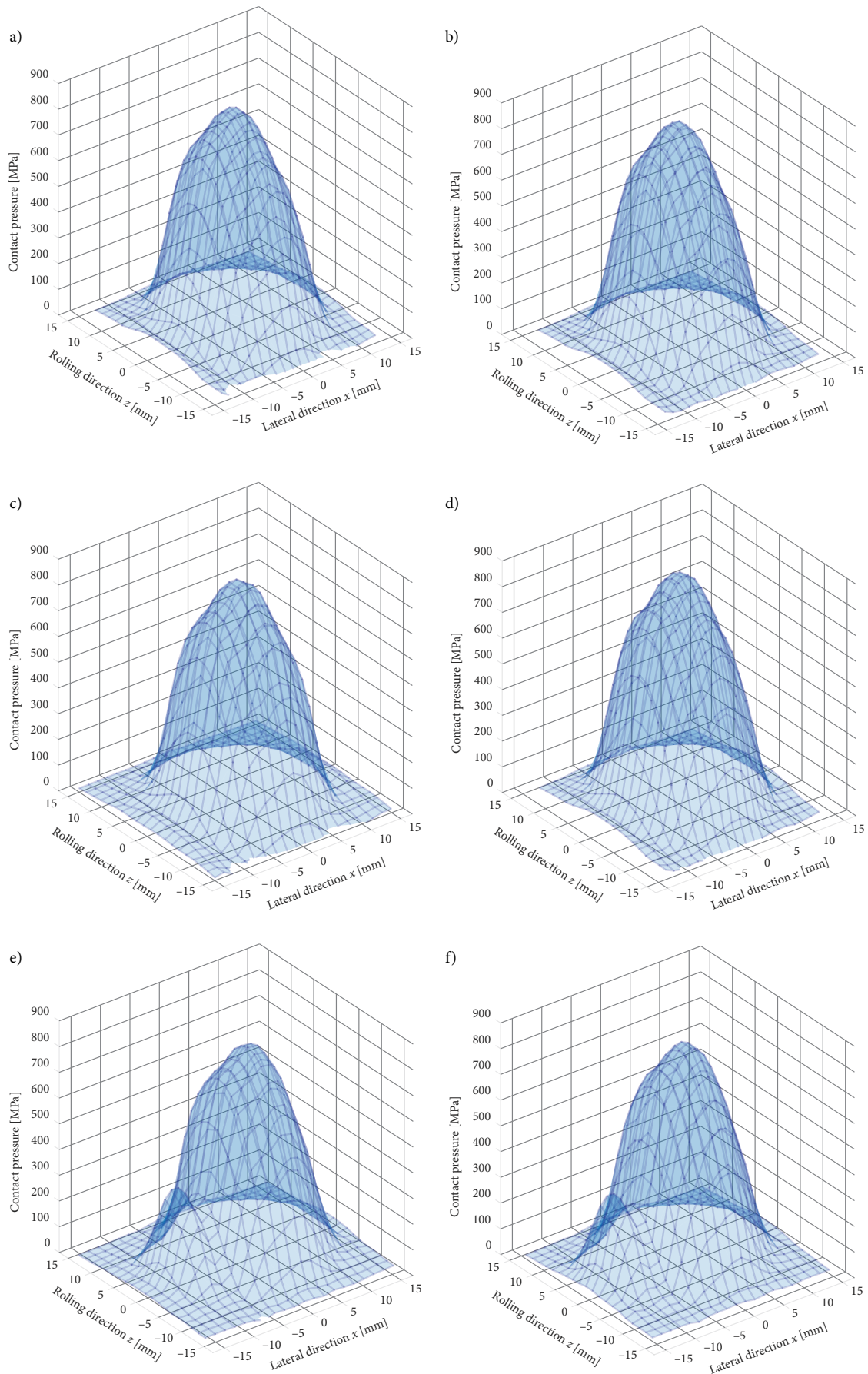


Figure 5. 3D distributions of contact pressure on the rail: a – $R = 2800$ m, rate-independent; b – $R = 2800$ m, rate-dependent; c – $R = 4000$ m, rate-independent; d – $R = 4000$ m, rate-dependent; e – $R = \infty$, rate-independent; f – $R = \infty$, rate-dependent

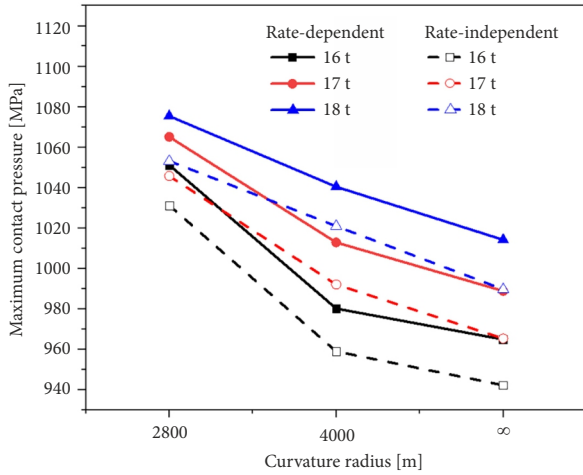


Figure 6. Maximum contact pressure values as a function of curvature radius

2.3.1. Tangential stress

The simulation moments at which the tangential stress components on the high and low rails reach a maximum under curve negotiation are at about 10 and 2.5 ms, respectively. While the tangential stress components for the left rail and right rail reach the maximum at around 7.5 and 7 ms under straight track case. The moment when the shear stress reaches the maximum nearly corresponds to the time of peak value for the wheel–rail contact force. The 3 stress components distribution along the rolling direction with axle load of 17 t is presented in Figure 10. It is evidently clear that the surface vertical stress σ_y is the largest, and then the longitudinal stress σ_z , followed by the lateral stress σ_x . The peak value of contact stress occurs at the center of the contact area due to not considering of creepage, and the stress is symmetrically distributed along the longitudinal direction. The 3 stress components increase significantly as the radius of the curve decrease. No matter what the condition, the maximum stress on the higher rail is larger than the lower rail. Otherwise, on the lower rail, the strain rate has obvious enhancement effect on longitudinal stress and lateral stress. On the higher rail, the strain rate has minor influence on the 3 stress components.

Under the axle load of 17 t, the distributions of the longitudinal stress in the longitudinal cross section and the lateral and vertical stresses in the lateral cross section of wheel–rail are illustrated in Figure 11. The maximum longitudinal and lateral stress both appear on the surface of the wheel–rail contact area, the maximum contact stress on the wheel tread is greater than that on the rail. The maximum values of the 3 stress components increase as the radius of the curve decreases, which aggravates the wear of the wheel and the rail. The influence of the axle load on the 3 stress components under wheel–rail contact area are also investigated, as shown in Figure 12. The maximum values of stress increases monotonously with the increasing axle load under 3 working conditions. The mag-

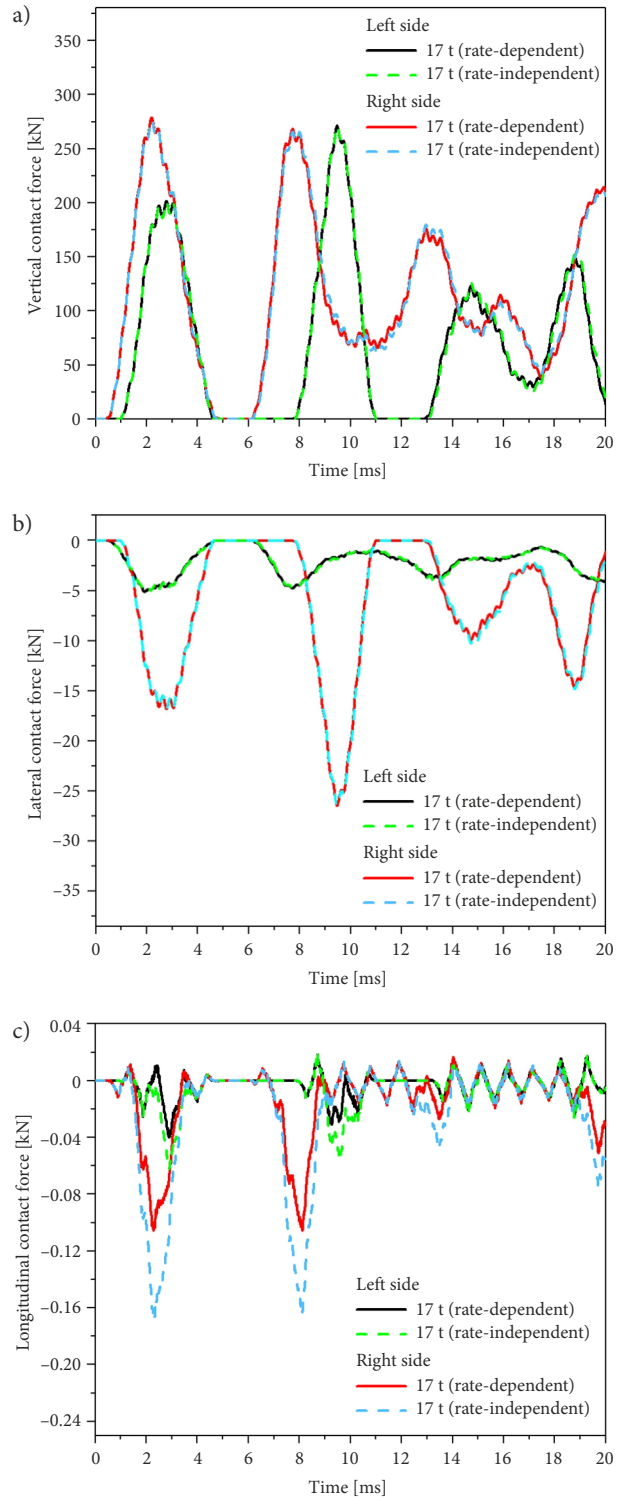


Figure 7. The typical wheel–rail contact force history curves: a – vertical contact force; b – lateral contact force; c – longitudinal contact force

nitude order of the 3 stress components is the same as that in Figure 10. Moreover, the maximum absolute values of the vertical and lateral stress are evidently sensitive to the strain rate, but the longitudinal is faintly sensitive to the strain rate under a curved track, which attested the correctness of the conclusion on the lower rail in Figure 10.

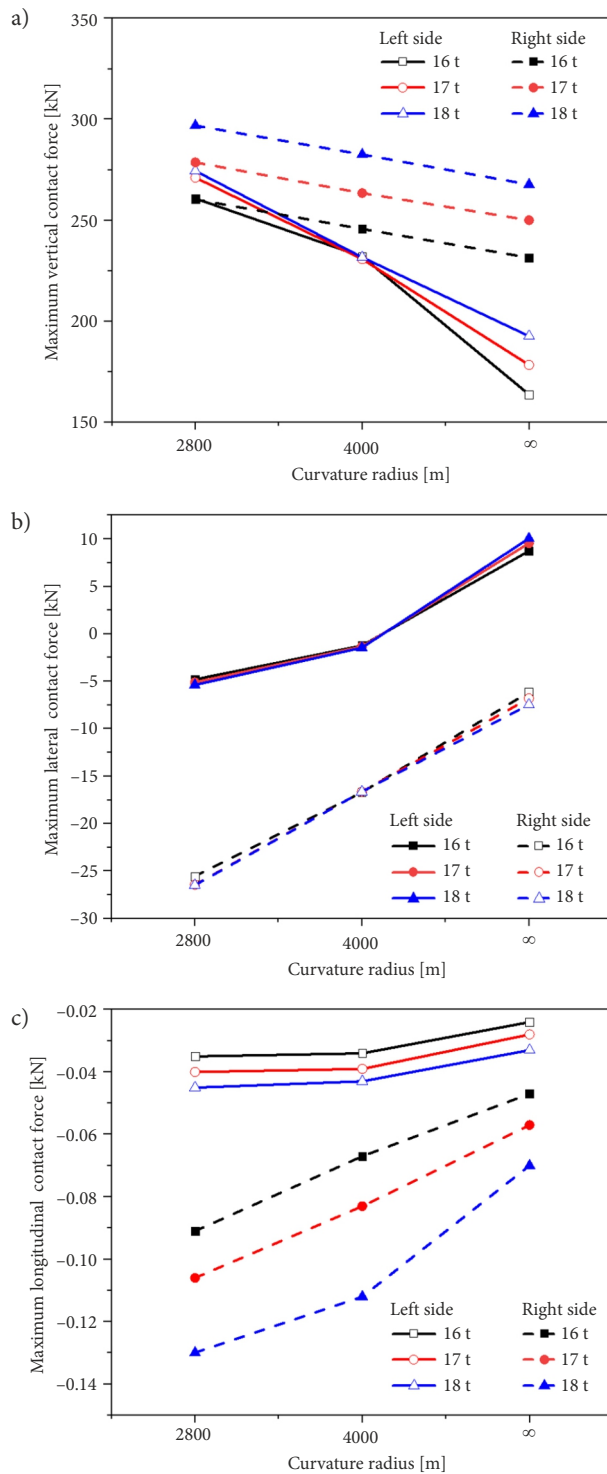


Figure 8. The maximum wheel–rail contact force under rate-dependent material model: a – vertical contact force; b – lateral contact force; c – longitudinal contact force

2.3.2. Von-Mises stress

The maximum von-Mises stress always occurs on the lower rail, and the distributions of von-Mises stress of the lower rail on the lateral cross sections for typical working conditions are investigated, as illustrated in Figure 13. Unlike the longitudinal and lateral stress distributions in Section 2.3.1, the maximum von-Mises stress always ap-

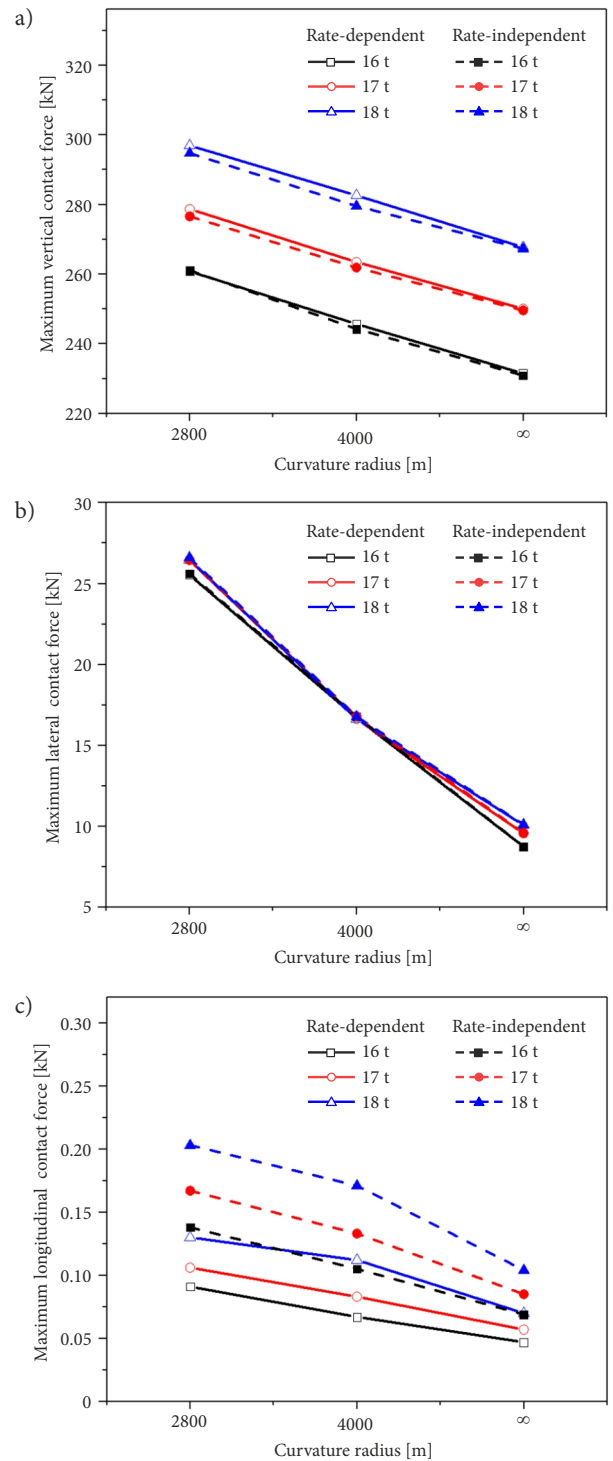


Figure 9. The absolute value of maximum wheel–rail contact force solved by 2 material models: a – vertical contact force; b – lateral contact force; c – longitudinal contact force

pears on the subsurface of the wheel–rail contact region, which ulteriorly demonstrate frictionless contact will be more likely to result in subsurface damage to the wheel and rail. The area of the von-Mises stress concentration region (red region) is larger on the curved track than that on the straight track; hence it will cause damage to a larger area on a curved track. The strain rate effect will make the

area of red region decrease. The distributions of von-Mises stress on the rail head for typical conditions are plotted in Figure 14a. As the difference of the superelevation and roll angle, the maximum von-Mises stress of the rail is 625 MPa at a curve radius of 2800 m, whereas 617 MPa at a curve radius of 4000 m in Figure 15, where both surpassed the yield stress of the rail steel material. The contours of the longitudinal cross section A-A and lateral cross sections B-B and C-C are illustrated in Figures 14b-d. It can be

observed that the area of the stress concentration region (red region) at the cross section B-B is larger than that at the cross section C-C. In addition, there are subtle deviations in depth, the stress concentration area on the cross section B is closer to the surface rail surface compared to cross section C-C, which can be distinctly reflected in Figure 14b along the longitudinal direction. The subsurface damage, such as (plastic flow, crack initiation and propagation) will be more likely to happen in higher stress region.

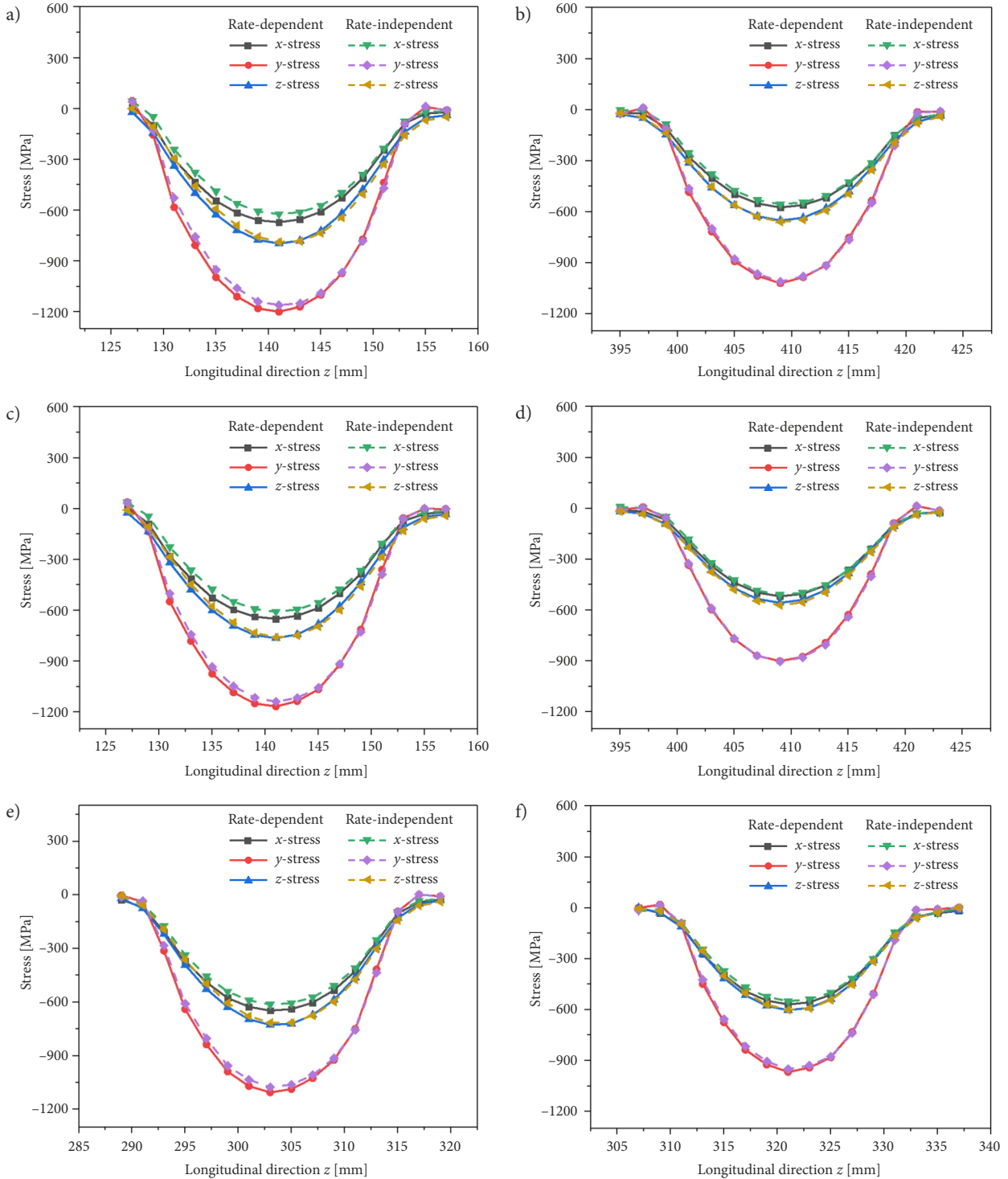


Figure 10. 3 stress components distribution along the rolling direction: a - $R = 2800$, lower rail; b - $R = 2800$ m, higher rail; c - $R = 4000$ m, lower rail; d - $R = 4000$ m, higher rail; e - $R = \infty$, right rail; f - $R = \infty$, left rail

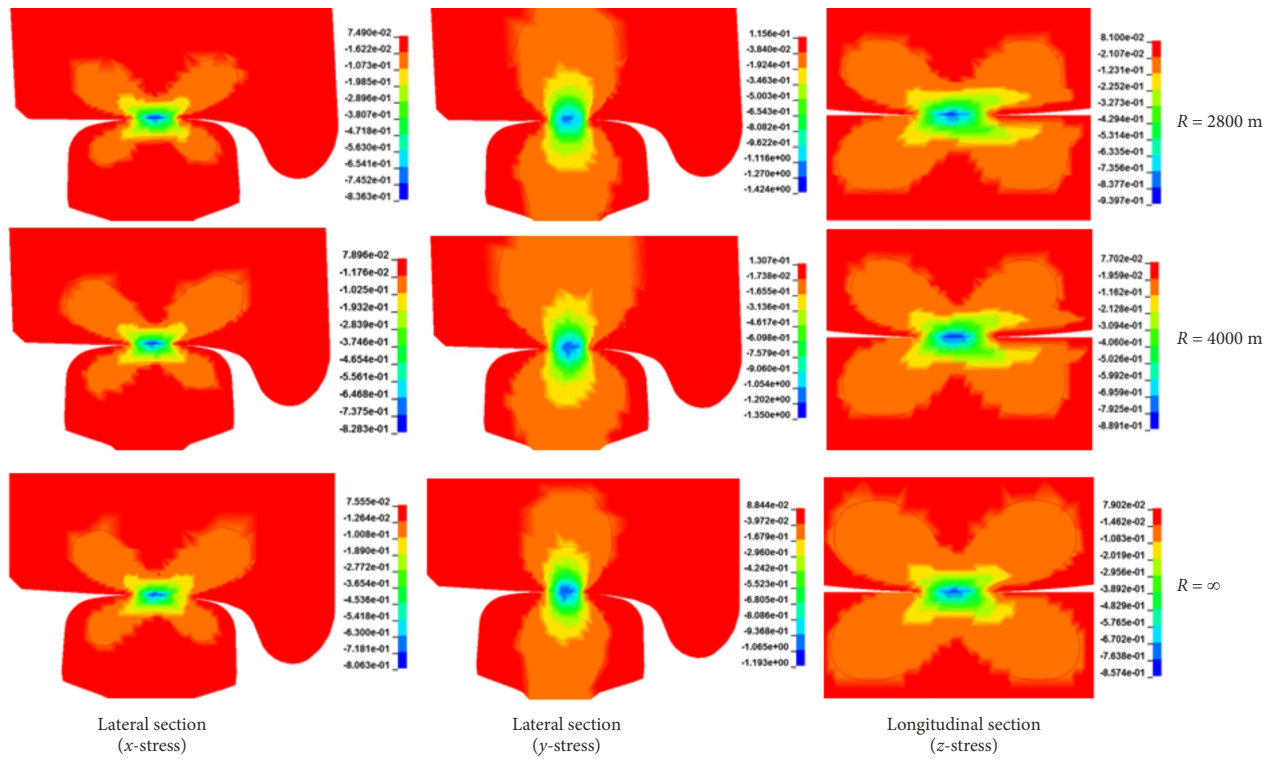


Figure 11. 3 stress components distribution on the cross section (rate-dependent)

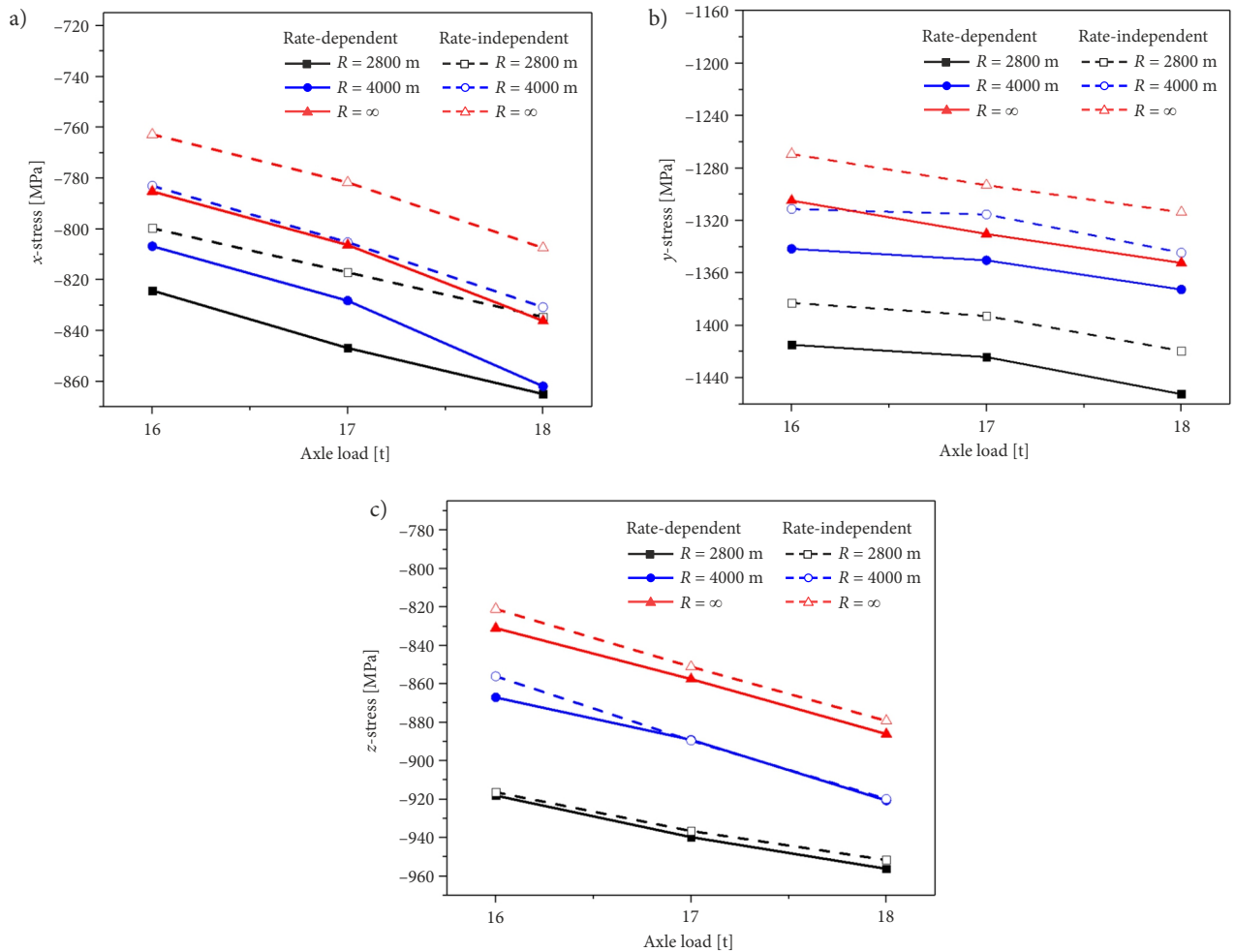


Figure 12. Maximum 3 stress components under different working conditions: a – x-stress; b – y-stress; c – z-stress

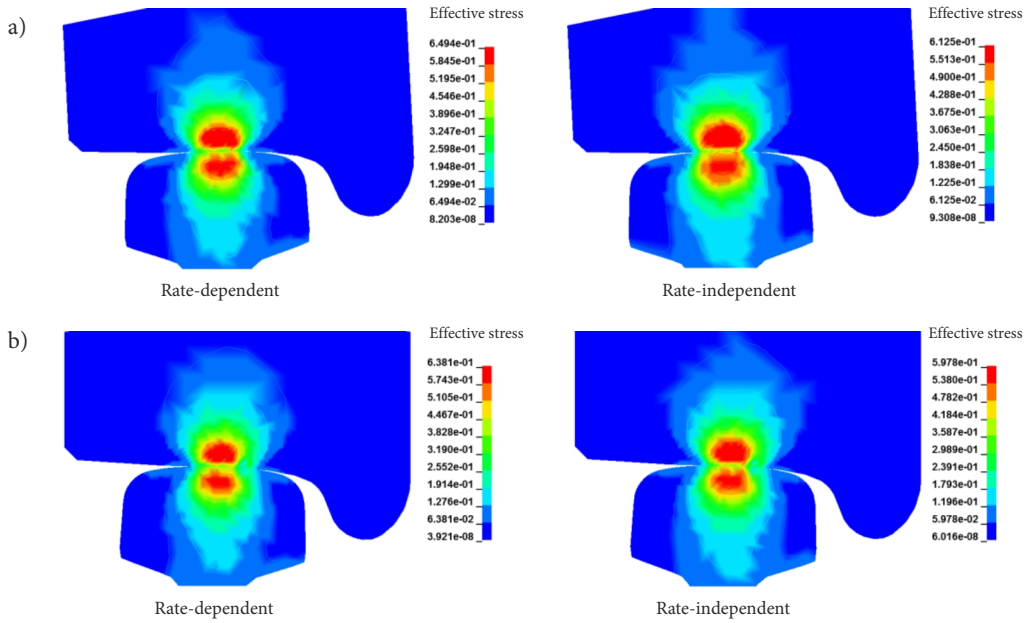


Figure 13. The von-Mises stress distributions under the axle load of 17 t: a - $R = 2800$ m; b - $R = \infty$

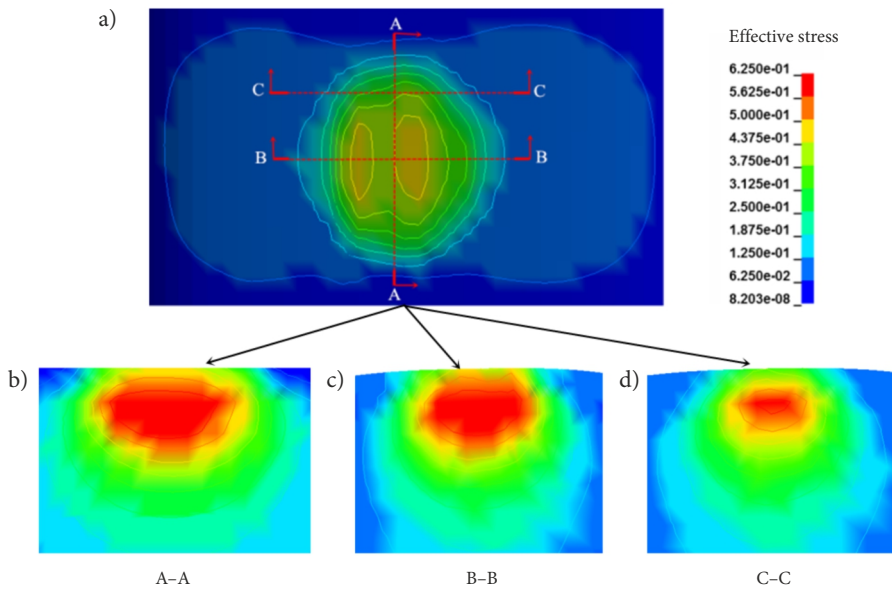


Figure 14. Von-Mises stress distribution with the curve radius of 2800 m (rate-dependent)

The maximum von-Mises stress under different axle loads and curvature radius are plotted in Figure 15. The maximum von-Mises stress on the wheel is also larger than that on the rail owing to the differences in wheel and rail materials. The maximum von-Mises stress increases as the curvature radius decreases under a constant axle load, and it monotonically increases as the axle load increases on a constant curve. Whenever it is on a straight or curved track, the strain rate hardening effect increases the von-Mises stress significantly.

2.3.3. Equivalent plastic strain

The distribution of equivalent plastic strain of the lower rail on the lateral cross section for typical condition is pre-

sented in Figure 16. Similar to the distribution of the maximum von-Mises stress, the maximum equivalent plastic strain on the wheel or rail appears inside it, which is from 2 to 5 mm from the contact surface. The strain rate effect also reduces the equivalent plastic strain zone under curve negotiation. The maximum equivalent plastic strain occurs on the rail and the equivalent plastic deformation zone on the rail is significantly larger than that on the wheel in Figure 16, which is mainly attributed to the fact that the yield strength of the rail steel is smaller than that of the rim. Therefore, the combination of large equivalent plastic strain and large plastic deformation region will result in a wider range of damage on the subsurface of the rail. Figure 17 compares the maximum equivalent plastic strain of the wheel and rail under different working conditions.

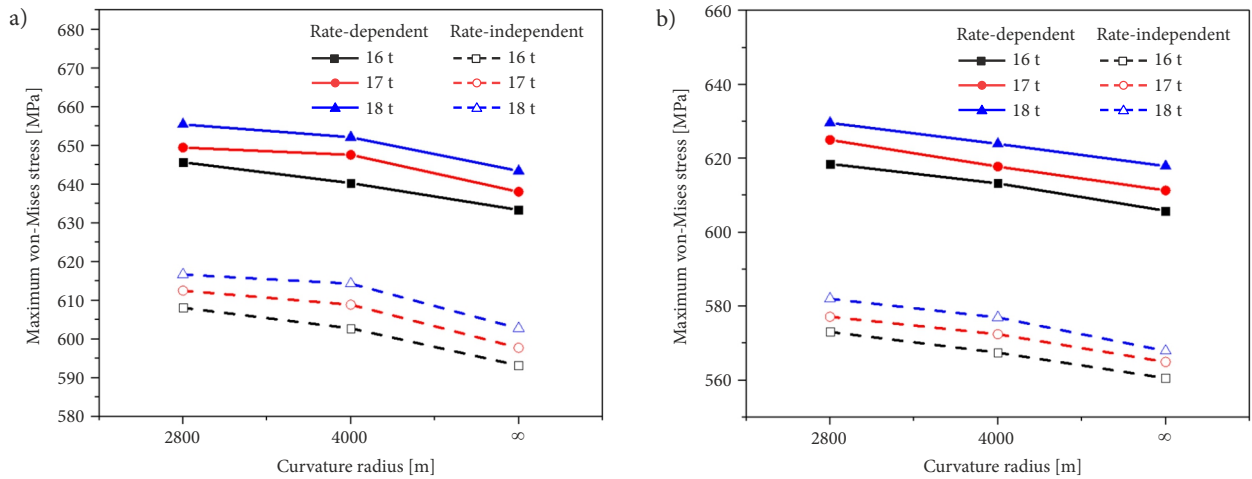


Figure 15. Maximum von-Mises stress as a function of curvature radius: a – wheel; b – rail

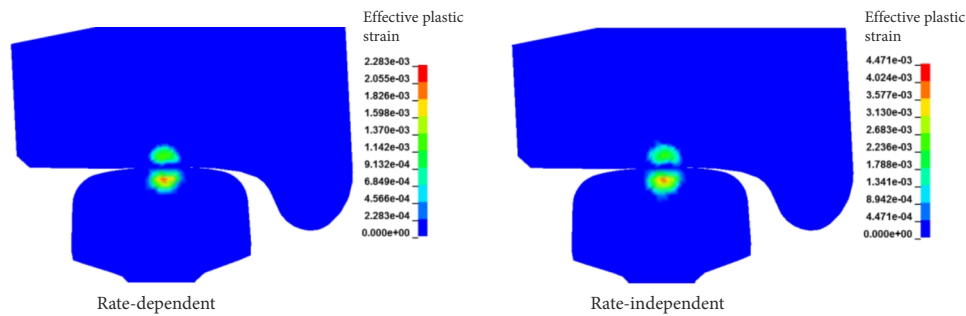


Figure 16. The distributions of equivalent plastic strain under the axle load of 17 t

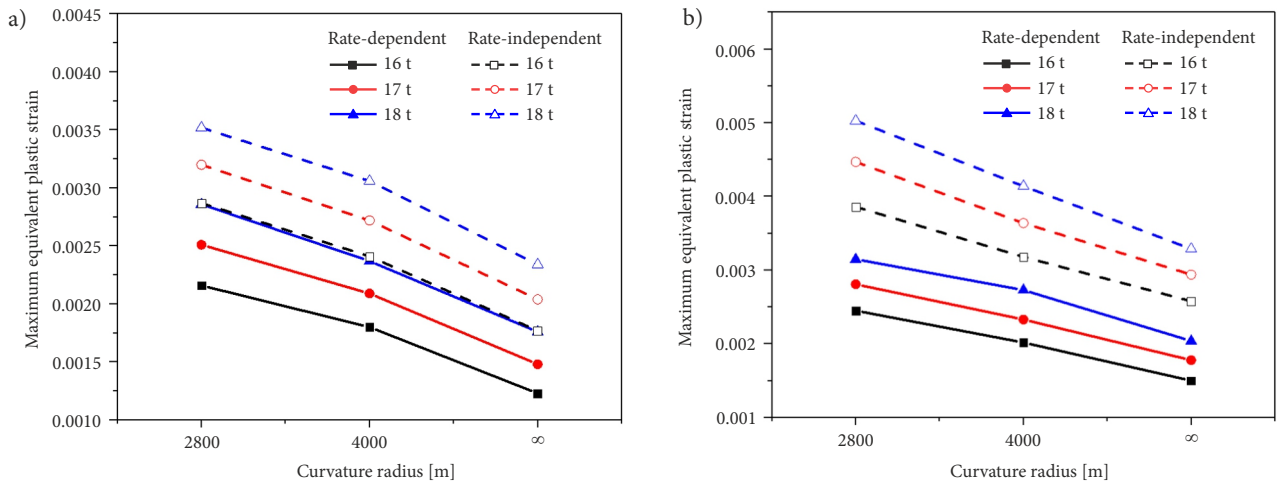


Figure 17. Maximum equivalent plastic strain as a function of curvature radius: a – wheel; b – rail

It can be seen that the maximum equivalent plastic strain increases monotonically with the increasing axle load and decreases as the radius of the curve increases. The maximum equivalent plastic strain of the wheel and rail are sensitive to the strain rate. Whether in a straight or curved track, the strain rate hardening effect can significantly inhibit plastic deformation of the wheel and rail.

2.3.4. RSF

Here, the effect of strain rate on dynamic wheel–rail response, in terms of von-Mises stress and equivalent plastic

strain, under the condition of complex wheel–rail contact of curve negotiation, was quantified by introducing a RSF. In addition, the value of RSF is given as:

$$RSF = \frac{\sigma_{\max, \text{rate-dependent}}}{\sigma_{\max, \text{rate-independent}}}, \quad (7)$$

or

$$RSF = \frac{\varepsilon_{\max, \text{rate-dependent}}}{\varepsilon_{\max, \text{rate-independent}}}. \quad (8)$$

Figure 18 describes the RSF for the wheel and rail, respectively, under different axle loads. The values of RSF of

wheel are smaller than those of the rail for the maximum von-Mises stress, whereas they are larger than those of the rail for equivalent plastic strain, which confirmed that the strain rate strengthening effect of the rail is greater than the wheel. Otherwise, it can be observed that the value of RSF on the straight track is larger than that on a curved track in regard to von-Mises stress and it is less than that on the curved track in regard to equivalent plastic strain. It may be due to the fact that the wheel–rail contact conditions are more complicated under the curved track, which weakens the strain rate hardening effect on the wheelset passing through a curved track.

2.4. The vertical acceleration response of the axle

The wheel–rail contact force will change due to the complexity of the contact geometry of curve negotiation, which will lead to the variation in the acceleration of axle. Figure 19 shows the vertical acceleration versus time history curves of 2 material models, under the curvature radius of 2800 m and axle load of 17 t. The acceleration history curves fluctuate greatly at the beginning, then the vibration amplitude gradually slows down and the acceleration

peak gradually stabilizes near the lower value. A certain distance is required to achieve the desired quasi-static state when the initial loads are exerted on the wheel–rail system in dynamic rolling contact simulation (Zhao, Li 2011), which account for the larger fluctuation occurs at the early stage. It also indicates that the strain rate has little effect on the acceleration of axle under a curved track. To further study the influences of axle load and curvature radius on the acceleration of the axle, early stage of large fluctuation is ignored due to the difficulty in filtering, see Figure 19. The average values of peak \bar{a}_p and through \bar{a}_t are introduced, and can be defined as:

$$\bar{a}_p = \frac{\sum_{i=1}^n a_p^i}{n}; \quad (9)$$

$$\bar{a}_t = \frac{\sum_{i=1}^m a_t^i}{m}, \quad (10)$$

where: n , m represents the number of selected peaks and troughs, respectively; a_p^i is the i -th peak; a_t^i is the i -th trough.

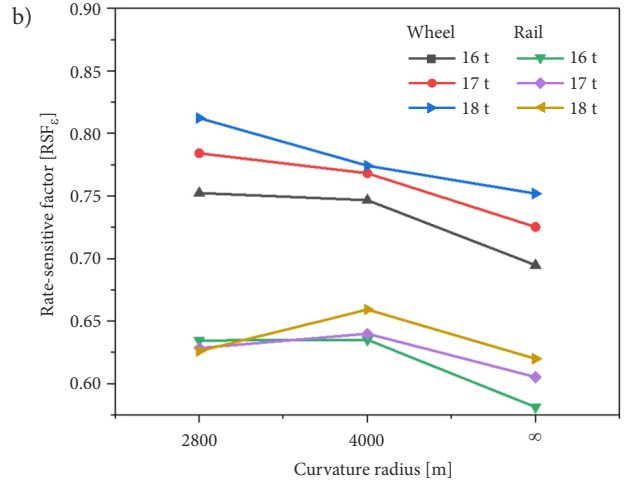
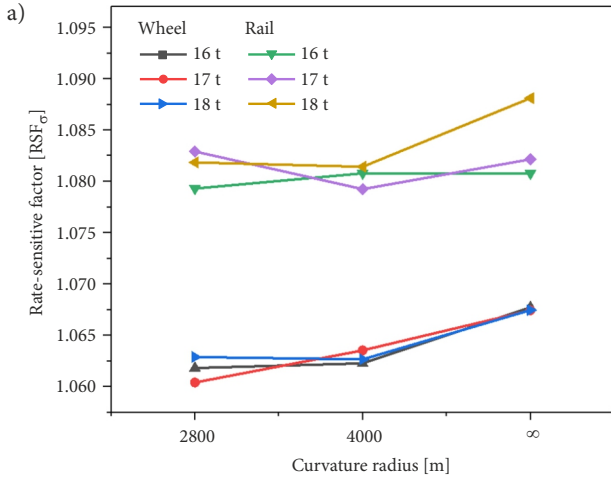


Figure 18. The RSF of the rail and wheel in terms of: a – von-Mises stress; b – equivalent plastic strain

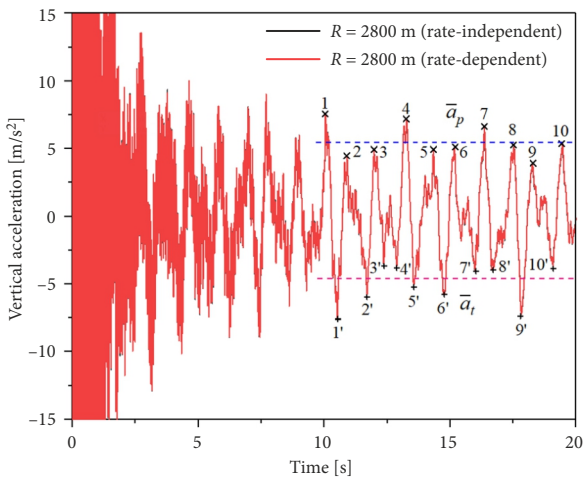


Figure 19. The vertical acceleration response history of 2 material models

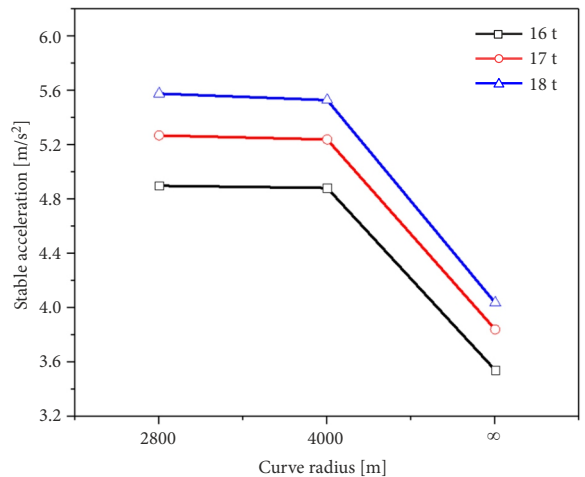


Figure 20. The stable acceleration as a function of curvature radius under various axle loads

Combining Equation (9) with Equation (10), the stable acceleration \bar{a} is written as:

$$\bar{a} = \frac{|\bar{a}_p| + |\bar{a}_t|}{2}. \quad (11)$$

The values of both n and m are equal to 10 in Figure 19. Since the strain rate has been demonstrated to have no effect on the acceleration, only the rate-independent case is considered here. The stable vertical accelerations for various axle loads are plotted in Figure 20. It increases as the axle load increases. The stable vertical acceleration on the curved track is about 1 m/s^2 higher than that on the straight track as the consequence of the superelevation.

Conclusions

In the present study, a 3D elastic-plastic FE model was created to simulate the dynamic wheel–rail contact behaviour of curve negotiation. The influences of axle load and curve radius as well as strain rate were also discussed, in terms of contact patch and contact pressure, wheel–rail contact force, contact stress and strain states and the acceleration of the axle. The obtained results can be concluded as follows:

- » the maximum contact pressure, vertical and longitudinal contact force, von-Mises stress and equivalent plastic strain increase monotonously with increasing axle load. However, the lateral wheel–rail contact force is insensitive to the axle load under a curved track. The maximum contact pressure, wheel–rail contact force, stress and strain increase as the radius of curvature decreases. The maximum stress and strain as well as maximum contact pressure appear on the lower rail side. The stable vertical acceleration of the axle on a curved track is larger than that of a straight track;
- » the strain rate effect can enhance the contact pressure and stress and suppress the plastic deformation of the wheel and rail. It has minor effect on the maximum vertical and lateral contact force as well as the acceleration of the axle. The strain rate sensitivity of the wheel and rail is weaker on the curved track than the straight track estimated by the RSF.

Acknowledgements

The authors greatly appreciate the financial supports by the:

- » National Natural Science Foundation of China (Grants No 12122211, 11772275);
- » Sichuan Science and Technology Program (Grant No 2019YJ0212);
- » Fundamental Research Funds for the Central Universities (Grant No 2682018CX69);
- » Research Fund of State Key Laboratory of Traction Power (Grant No 2019TPL-T11).

Disclosure statement

No potential conflict of interest was reported by the authors.

References

- Boocock, D. 1969. Steady-state motion of railway vehicles on curved track, *Journal of Mechanical Engineering Science* 11(6): 556–566.
https://doi.org/10.1243/JMES_JOUR_1969_011_069_02
- BS EN 13104:2009+A1:2010. *Railway Applications. Wheelsets and Bogies. Powered Axles. Design Method.*
- Dailydka, S.; Lingaitis, L. P.; Myamlin, S.; Prichodko, V. 2008. Modelling the interaction between railway wheel and rail, *Transport* 23(3): 236–239.
<https://doi.org/10.3846/1648-4142.2008.23.236-239>
- Elkins, J. A.; Gostling, R. J. 1977. A general quasi-static curving theory for railway vehicles, *Vehicle System Dynamics: International Journal of Vehicle Mechanics and Mobility* 6(2–3): 100–106. <https://doi.org/10.1080/00423117708968515>
- Han, L.; Jing, L.; Zhao, L. 2018. Finite element analysis of the wheel–rail impact behavior induced by a wheel flat for high-speed trains: The influence of strain rate, *Proceedings of the Institution of Mechanical Engineers, Part F: Journal of Rail and Rapid Transit* 232(4): 990–1004.
<https://doi.org/10.1177/0954409717704790>
- Hertz, H. 1882. Ueber die Berührung fester elastischer Körper, *Journal für die reine und angewandte Mathematik* 92: 156–171.
<https://doi.org/10.1515/9783112342404-004> (in German).
- Jing, L.; Han, L. 2017. Further study on the wheel–rail impact response induced by a single wheel flat: the coupling effect of strain rate and thermal stress, *Vehicle System Dynamics: International Journal of Vehicle Mechanics and Mobility* 55(12): 1946–1972. <https://doi.org/10.1080/00423114.2017.1340651>
- Jing, L.; Han, L.; Zhao, L.; Zhang, Y. 2016. The dynamic tensile behavior of railway wheel steel at high strain rates, *Journal of Materials Engineering and Performance* 25(11): 4959–4966.
<https://doi.org/10.1007/s11665-016-2359-y>
- Jing, L.; Su, X.; Zhao, L. 2017. The dynamic compressive behavior and constitutive modeling of D1 railway wheel steel over a wide range of strain rates and temperatures, *Results in Physics* 7: 1452–1461. <https://doi.org/10.1016/j.rinp.2017.04.015>
- Jing, L.; Liu, Z.; Liu, K. 2022a. A mathematically-based study of the random wheel–rail contact irregularity by wheel out-of-roundness, *Vehicle System Dynamics: International Journal of Vehicle Mechanics and Mobility* 60(1): 335–370.
<https://doi.org/10.1080/00423114.2020.1815809>
- Jing, L.; Su, X.; Feng, C.; Zhou, L. 2022b. Strain-rate dependent tensile behavior of railway wheel/rail steels with equivalent fatigue damage: experiment and constitutive modeling, *Engineering Fracture Mechanics* 275: 108839.
<https://doi.org/10.1016/j.engfracmech.2022.108839>
- Kaewunruen, S.; Ngamkhanong, C.; Liu, X. 2019. Spectro-temporal responses of curved railway tracks with variable radii of arc curves, *International Journal of Structural Stability and Dynamics* 19(4): 1950044.
<https://doi.org/10.1142/S0219455419500445>
- Kalker, J. J. 1967. *On the Rolling Contact of Two Elastic Bodies in the Presence of Dry Friction.* PHD thesis, Delft University of Technology, Netherlands. 170 p. Available from Internet: <https://repository.tudelft.nl/islandora/object/uuid%3Aaa44829b-c75c-4abd-9a03-fec17e121132>
- Kalker, J. J. 1973. Simplified theory of rolling contact, *Delft Progress Report Series C* 1(1): 1–10.
- Liu, P.-F.; Zhai, W.-M.; Wang, K.-Y.; Feng, Q.-B.; Chen, Z.-G. 2018a. Theoretical and experimental study on vertical dynamic characteristics of six-axle heavy-haul locomotive on curve, *Transport* 33(1): 291–301.
<https://doi.org/10.3846/16484142.2016.1180638>

- Liu, W. F.; Du, L.; Liu, W. N.; Thompson, D. J. 2018b. Dynamic response of a curved railway track subjected to harmonic loads based on the periodic structure theory, *Proceedings of the Institution of Mechanical Engineers, Part F: Journal of Rail and Rapid Transit* 232(7): 1932–1950. <https://doi.org/10.1177/0954409718754470>
- Ma, W.; Xu, Z.; Luo, S.; Song, R. 2015. Influence of wheel axle stiffness character to the wheel/rail dynamic contact on the straight track, *Transport* 30(1): 24–32. <https://doi.org/10.3846/16484142.2013.819035>
- Ma, X.; Jing, L.; Han, L. 2018. A computational simulation study on the dynamic response of high-speed wheel–rail system in rolling contact, *Advances in Mechanical Engineering* 10(11): 1–11. <https://doi.org/10.1177/1687814018809215>
- Matsumoto, A.; Sato, Y.; Nakata, M.; Tanimoto, M.; Qi, K. 1996. Wheel–rail contact mechanics at full scale on the test stand, *Wear* 191(1–2): 101–106. [https://doi.org/10.1016/0043-1648\(95\)06710-8](https://doi.org/10.1016/0043-1648(95)06710-8)
- Matsumoto, A.; Sato, Y.; Ohno, H.; Mizuma, T.; Suda, Y.; Tanimoto, M.; Oka, Y. 2006. Study on curving performance of railway bogies by using full-scale stand test, *Vehicle System Dynamics: International Journal of Vehicle Mechanics and Mobility* 44: 862–873. <https://doi.org/10.1080/00423110600907402>
- Mosayebi, S.-A.; Zakeri, J.-A.; Esmaeili, M. 2016. Some aspects of support stiffness effects on dynamic ballasted railway tracks, *Periodica Polytechnica Civil Engineering* 60(3): 427–436. <https://doi.org/10.3311/PPci.7933>
- Mosayebi, S.-A.; Zakeri, J.-A.; Esmaeili, M. 2017. Vehicle/track dynamic interaction considering developed railway substructure models, *Structural Engineering and Mechanics* 61(6): 775–784. <https://doi.org/10.12989/sem.2017.61.6.775>
- Newland, D. E. 1968. Steering characteristics of bogie, *Railway Gazette* 124: 745–750.
- Rezvani, M. A.; Owhadi, A.; Niksai, F. 2009. The effect of worn profile on wear progress of rail vehicle steel wheels over curved tracks, *Vehicle System Dynamics: International Journal of Vehicle Mechanics and Mobility* 47(3): 325–342. <https://doi.org/10.1080/00423110802108957>
- Sladkowski, A.; Sitarz, M. 2005. Analysis of wheel–rail interaction using FE software, *Wear* 258(7–8): 1217–1223. <https://doi.org/10.1016/j.wear.2004.03.032>
- Su, X.; Zhou, L.; Jing, L.; Wang, H. 2020. Experimental investigation and constitutive description of railway wheel/rail steels under medium-strain-rate tensile loading, *Journal of Materials Engineering and Performance* 29(3): 2015–2025. <https://doi.org/10.1007/s11665-020-04720-1>
- TB 10621-2014. *Code for Design of High speed Railway*. Chinese Standard (in Chinese).
- Telliskivi, T.; Olofsson, U. 2001. Contact mechanics analysis of measured wheel–rail profiles using the finite element method, *Proceedings of the Institution of Mechanical Engineers, Part F: Journal of Rail and Rapid Transit* 215(2): 65–72. <https://doi.org/10.1243/0954409011531404>
- Vo, K. D.; Tieu, A. K.; Zhu, H. T.; Kosasih, P. B. 2014. A 3D dynamic model to investigate wheel–rail contact under high and low adhesion, *International Journal of Mechanical Sciences* 85: 63–75. <https://doi.org/10.1016/j.ijmecsci.2014.05.007>
- Vo, K. D.; Zhu, H. T.; Tieu, A. K.; Kosasih, P. B. 2015. FE method to predict damage formation on curved track for various worn status of wheel/rail profiles, *Wear* 322–323: 61–75. <https://doi.org/10.1016/j.wear.2014.10.015>
- Wang, K.; Huang, C.; Zhai, W.; Liu, P.; Wang, S. 2014. Progress on wheel-rail dynamic performance of railway curve negotiation, *Journal of Traffic and Transportation Engineering* 1(3): 209–220. [https://doi.org/10.1016/S2095-7564\(15\)30104-5](https://doi.org/10.1016/S2095-7564(15)30104-5)
- Wang, W. J.; Guo, J.; Liu, Q. Y.; Zhu, M. H.; Zhou, Z. R. 2009. Study on relationship between oblique fatigue crack and rail wear in curve track and prevention, *Wear* 267(1–4): 540–544. <https://doi.org/10.1016/j.wear.2008.12.100>
- Yang, Z.; Li, Z.; Dollevoet, R. 2016. Modelling of non-steady-state transition from single-point to two-point rolling contact, *Tribology International* 101: 152–163. <https://doi.org/10.1016/j.triboint.2016.04.023>
- Zakeri, J. A.; Tajalli, M. R. 2018. Comparison of linear and non-linear behavior of track elements in contact-impact models, *Periodica Polytechnica Civil Engineering* 62(4): 963–970. <https://doi.org/10.3311/PPci.12058>
- Zboński, K. 1998. Dynamical investigation of railway vehicles on a curved track, *European Journal of Mechanics – A/Solids* 17(6): 1001–1020. [https://doi.org/10.1016/S0997-7538\(98\)90506-X](https://doi.org/10.1016/S0997-7538(98)90506-X)
- Zhai, W.; Wang, K.; Cai, C. 2009. Fundamentals of vehicle–track coupled dynamics, *Vehicle System Dynamics: International Journal of Vehicle Mechanics and Mobility* 47(11): 1349–1376. <https://doi.org/10.1080/00423110802621561>
- Zhao, X.; Li, Z. 2011. The solution of frictional wheel–rail rolling contact with a 3D transient finite element model: validation and error analysis, *Wear* 271(1–2): 444–452. <https://doi.org/10.1016/j.wear.2010.10.007>
- Zhou, X.; Wang, J.; Jing, L. 2022. Coupling effects of strain rate and fatigue damage on wheel-rail rolling contact behaviour: a dynamic finite element simulation, *International Journal of Rail Transportation* 1–22. <https://doi.org/10.1080/23248378.2022.2083711>